García Martínez, A.; Monsalve Serrano, J.; Heuser, B.; Jakob, M.; Kremer, F.; Pichinger, S. (2016). Influence of fuel properties on fundamental spray characteristics and soot emissions using different tailor-made fuels from biomass. Energy Conversion and Management. 108:243-254. doi:10.1016/j.enconman.2015.11.010.

Influence of fuel properties on fundamental spray characteristics and soot emissions using different tailor-made fuels from biomass

Energy Conversion and Management, Volume 108, 15 January 2016, Pages 243–254.
http://dx.doi.org/10.1016/j.enconman.2015.11.010

Antonio García [a,]*, Javier Monsalve-Serrano[a], Benedikt Heuser[b], Markus Jakob[c], Florian Kremer[b], Stefan Pischinger[b]

a- CMT - Motores Térmicos, Universitat Politècnica de València, Camino de Vera s/n, 46022 Valencia, Spain

b- Institute for Combustion Engines, RWTH Aachen University, Aachen, Germany

c- before Institute for Combustion Engines, RWTH Aachen University, Aachen, Germany, now FEV GmbH, Aachen

(*) Corresponding author: angarma8@mot.upv.es (Antonio García Martínez)

Abstract

This work evaluates the potential of some new biomass-derived fuels as candidates for compression ignition operation. Thus, fundamental spray characteristics related to fuel vaporization and fuel/air mixing process for 2-Methyltetrahydrofuran, Di-n-butyl ether and 1-octanol has been studied and compared with conventional EN590 Diesel fuel. For this purpose, OH* chemiluminescence and shadowgraphy measurements in a high pressure chamber as well as 1D simulations with a spray model have been carried out at different operating conditions representative of the NEDC driving cycle. Finally, measured soot emissions in the single-cylinder engine were presented and discussed.

Results from the high pressure chamber presented very good agreement in terms of liquid length and vapor penetration with simulation results. Thus, some analytical expressions related to macroscopic spray characteristics have been proposed and validated experimentally for all four fuels. Finally, the single-cylinder engine results confirmed the relevant role of soot formation on final emissions for 1-octanol and 2-MTHF. In addition, DNBE showed greater soot oxidation potential than diesel and other TMFB candidates.

Keywords

1-octanol, DNBE, 2-MTHF, High temperature vessel, spray modelling

1. Introduction

The extensive use of internal combustion engines (ICE) to cover fundamental requirements such as people and goods transportation and power generation has result in their mass production [1]. In spite of their potential, it is well-known that conventional mixing-controlled diesel combustion in compression ignition (CI) engines results in unacceptable raw NOx and soot emissions [2]-[4]. Thus, complex and costly aftertreatment devices are needed to meet

the targets imposed by the current emissions regulations [5][6]. This fact, together with the finite nature and instability of fossil fuel supply [7]-[10], has led to extensive research on alternative fuels which shall contribute to modern combustion systems to reduce both engine emissions and the dependence of ICEs on fossil fuels [11]. In this sense, an imperative long-term goal for the scientific community is to determine the optimal combination of fuel production processes based on renewable raw materials and their utilization in optimized ICEs.

The use of oxygenated fuel compounds has shown a positive impact on engine-out emissions from conventional mixing-controlled combustion. Recent studies demonstrated that biodiesel fuel allows a consistent reduction of particulate matter (PM) emissions versus conventional diesel [12]. The analysis of spray mixing, vaporization and combustion processes of biodiesel fuel in optical research engines and combustion test rigs allowed to explain the main reasons of the soot emissions reduction [13]. In particular, it was found that because of fuel oxygenation, mixtures are less fuel rich at the center of the jet for biodiesel. Consequently, premixed combustion occurs at lower stoichiometry, closer to the jet center, and confined by a more narrow diffusion flame. The longer time for soot inception and growth, combined with entrained oxygen during this period, ultimately limits the soot formation significantly for biodiesel compared to diesel [14].

More recently, several oxygenated fuels derived from biomass have been identified to be suitable for CI operation. In particular, Decanol has been widely studied in a single-cylinder research engine under conventional mixing-controlled combustion conditions showing up to 90% reduced soot emissions than diesel fuel depending on the engine load point [15]. Moreover, the influence of several oxygenated fuels on homogeneous direct injection combustion were investigated using 2-Methyltetrahydrofuran (2-MTHF), 1-Butanol and 2-Butanol [16]. In this case, results showed that these fuels do not provide significant improvements for homogeneous lean burn combustion despite a significant reduction in NOx emissions. The major difference found between these fuels was the knock resistance, which allowed increased thermal efficiency with 2-Butanol through the increase in compression ratio. In addition to the already mentioned fuels, some other biomass-derived components such as Di-n-butyl ether (DNBE) and 1-octanol were also identified as promising candidates for CI operation [17][18]. These fuel candidates feature a high oxygen content together with a rather low boiling point compared to Diesel fuel, which has been shown as a promising way to contribute to a significant reduction in engine-out smoke at various load and speed conditions even with lower engine-out NOx emissions [19]-[21].

Aside from experimentation, one-dimensional (1D) spray models have been quite often used for the prediction of free spray evolution under steady boundary conditions. Due to the low computational requirements, local flow thermodynamics can be calculated with very high detail, which enables different approaches for the spray analysis. In 2008, Pastor et al. [22][23] presented a 1D model with a general formulation that enables the prediction of any type of spray flow, under both inert and reacting conditions. Furthermore, due to the mixing-controlled hypothesis upon which the model is based, it can be used for the description of both a gas jet and also a diesel spray working under real engine conditions. By making some assumptions derived from the theory of turbulent gas jets, the model enables the estimation of the distribution of properties within the spray (composition, temperature, density, etc.), as well as the tip penetration. This model has been used in literature for complementing studies developed in combustion vessels [24], optical engines [25] and single-cylinder research engines [26]. In 2009, Musculus and Kattke [27] also proposed a 1D model for transient diesel jet with the aim to understand the jet mixing process in case of unsteady injection rate. This was an extension of the Naber and Siebers model and some simplifying assumptions were made based on experimental observations [28]. The model results allowed explaining the formation of fuel-lean regions near the injector after the end of injection (EOI). Moreover, the model

indicated the presence of an "entrainment wave" that travels along the jet from upstream, promoting fuel air mixing after EOI. This model has been also used to explain results obtained by means of combustion vessels [14] and optical single-cylinder research engine [29][30].

The main objective of the present research is to study the mixture formation of several fuels derived from biomass, 2-MTHF, DNBE and 1-octanol, to gain understanding on the mechanisms for their low soot emissions. For this purpose, fundamental spray characteristics such as liquid length (LL) and lift-off length (LOL) have been determined by applying simultaneous measurements of OH* chemiluminescence and shadowgraphy in a high pressure chamber (HPC). Moreover, the 1D spray model proposed by Pastor et al. has been used to complement the experimental information. Finally, in order to validate the findings extracted from the fundamental study under realistic conditions, several soot measurements using a single-cylinder engine (SCE) are presented.

2. Experimental facility

2.1. High pressure chamber

The optical measurements are conducted at a continuously scavenged HPC test-bench [31]. During operation, a constant air volume-flow of V = 50m_n^3/h (where the subscript *n* stands for normal conditions) enters the HPC from the bottom side with a maximum pressure of P_{max} = 140 bar. Since the resulting air velocity inside the vessel is below 0.1 m/s, no significant influence on combustion process is expected. This flow is heated by two electrical cartridges connected in series in the lower test-bench section before entering the measurement volume. Therefore, maximum steady-state temperatures of T_{max} = 1000 K can be generated, which allows the simulation of a wide range of boundary conditions inside the measurement volume. This volume is accessible by all four horizontal sides. One of these accesses is occupied by the mounted injector, while the three other sides of the measurement volume are equipped with 120 mm silica windows. Therefore, simultaneous optical techniques can be applied in the HPC test-bench. After flowing through the chamber, the air is cooled down, depressurized, and guided through an exhaust after-treatment system.

2.2. Injection system

The injection system used a series production piezo-actuated injector equipped with an equiangular 3-hole nozzle. This nozzle design is used to avoid optical overlay of neighboring spray cones from a side view. The main characteristics of the nozzle hole geometry are depicted in table 1.

Parameter	Value
Nozzle type	Mini sac
Number of holes	3 (120° spacing)
Orifice diameter [µm]	118
ks-factor	1.3
Cone angle [°]	148

Table 1. Details of nozzle configuration.

The injector is energized by a power-unit with a pull-in current set to 17 A for 300 µs, and holding current set to 12 A. Moreover, the hydraulic delay of the injector, which was determined by light scattering and rate measurements, is 360 µs. In addition, the fuel is pressurized using a piston pump, and the injector is connected to the rail via 2 m long high pressure tube. Furthermore a piezoresistive high pressure sensor (0 bar - 2000 bar) is mounted close to the injector.

2.3. Fuels

In general, biomass consists of lignocellulose, what is a complex of the three biopolymers cellulose, hemicellulose, and lignin. Within the Aachen-based research group, the production pathways for the tailor-made fuels from biomass (TMFB) rely on the selective (bio-) chemical transformation processes of lignocellulosic biomass, retaining nature's synthetic effort to the extent possible. Therefore, several pathways are developed for the selective and effective chemical conversion of biomass. In a first step, the lignocellulose is split up into its components. In succession, innovative reaction media such as ionic liquids are used to break up the linkages between these components and to separate the respective fractions. Then, the individual components can be converted into the desired fuel molecules using various catalytic conversion methods. In this sense, figure 1 shows possible methods of converting the lignocellulose fractions via selected intermediates into the desired fuel components. Depending on the chosen pathway and the targeted intermediate/platform molecule, a large variety of different fuel compounds can be produced from cellulosic biomass with a high selectivity. Thus, DNBE can be synthesized via etherification of n-butanol, 2-MTHF can be obtained through the catalytic hydrogenation of levulinic acid and 1-octanol can be produced from the biomass based platform molecules furfural and acetone [32]-[34].

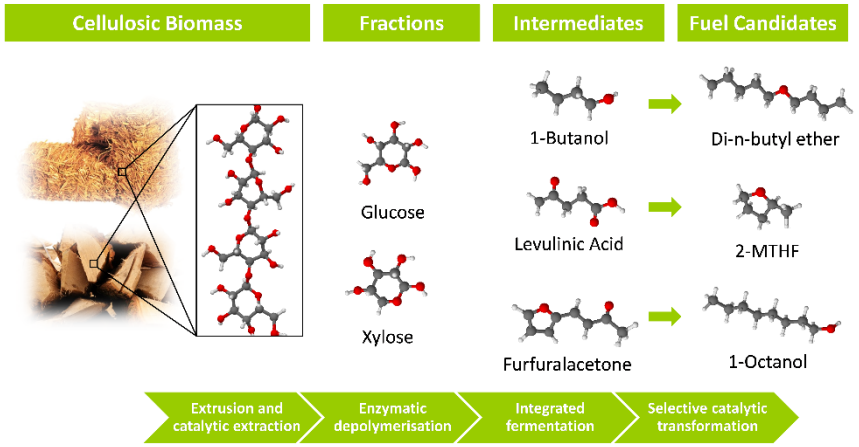

Figure 1. Production pathways of TMFB.

The more relevant chemical and physical characteristics of 1-octanol, 2-MTHF and DNBE related to diesel type combustion are listed in table 2. The properties of the reference diesel fuel are also depicted.

	Diesel	1-octanol	2-MTHF	DNBE
Boiling temperature [°C][35]	180-350	195	80	141
Heating value [MJ/kg][36]	42.7	37.6	33.5	38.3
Density [kg/m^3] @ 25 °C[37]	833	823	858.02	764
Cetane number [-][38]	53	39.1	~15	~100
Oxygen content [% m/m]	0.75	12.3	18.6	12.3
Vapor Pressure [mbar] @ 20 °C[35]	<1	0.031	136	6.4
Surface Tension [mN/m] @ 25 °C[38]	20.5	27.2	22.8	22.4
Dynamic Viscosity [mPa s] @ 40 °C[40]	3	4.379	0.35959	0.51367
Enthalpy of Vaporization [kJ/kg] @ 25 °C[40]	358	555.7	390.4	352.7

Table 2. Fuel characteristics.

2.4. Optical set-up

Figure 2 shows the optical set-up at the HPC test-bench for the simultaneous application of OH* chemiluminescence visualization and shadowgraphy technique. Both cameras are positioned on the same side of the test-bench. Since the investigated spray-cone propagates through the measurement volume diagonally, both cameras are tilted by 45°.

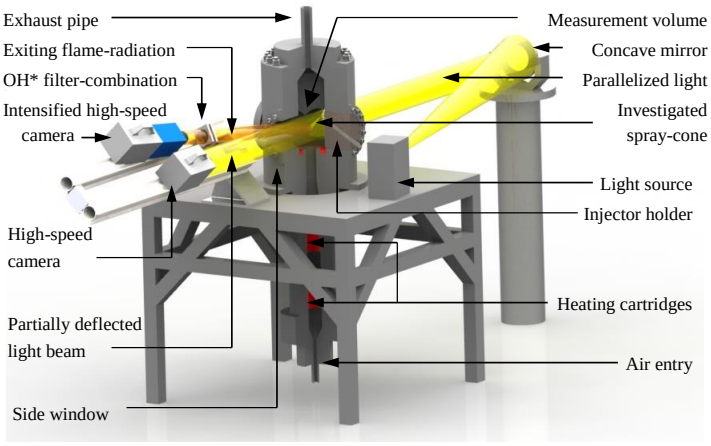

Figure 2. Optical set-up for the simultaneous application of OH* chemiluminescence visualization and shadowgraphy technique in the high pressure chamber [41].

The experimental investigations have been done at the continuously scavenged high-pressure chamber (HPC) for diesel engine related investigations at RWTH Aachen University. A cut section fo the test-bench as well as the optical setup for the optical measurements in this publication are shown in figure 2. The test-bench works with a continuous air flow of 50 m_n^3/h, which enters the chamber with 140 bar at the bottom side. This air flow is heated by two electrical cartridges in the lower test-bench section before entering the measurement volume, which can reach 140 bar and 1000 K [31]. During the tests for this publication, the measurement volume is equipped with circular windows at three side of the measurement volume and an injector holder at the fourth side. The injector, which is applied to the holder is equipped with an equiangular three hole nozzle, which is required to visualize one individual spray cone completely. The equiangular design furthermore avoids needle tilting during operation. The injector holder is designed to direct the investigated spray diagonally through the measurement volume [31].
The optical set-up consists of the parts for shadowgraphic and chemiluminscent visualization. The shadowgraphic set-up includes the light source, concave mirror and an intensified high-speed camera. The light source is a 150W Xenon-steam lamp, which is operated at 90% power to increase life-time. The concave mirror has a focal length of 1400 mm, which equals the adjusted distance between light source and mirror. Therefore, the light beams are parallelized in direction before entering the measurement volume. Within the measurement volume, the light beams are deflected in direction by passing the contact surface of gaseous media with different density in non-perpendicular direction. In addition to this, light beams are also scattered out the shadowgraphic line of sight by droplets in the area of liquid spray penetration. In consequence, the shadowgraphic setup allows a precise determination about the hydrodynamical spray developments.
In order to determine the ignition delay, the experimental setup is extended by an intensified

high-speed camera, which is equipped with the filter combination described by Pauls et al. [40]. Therefore, the camera detects only radiation in the wavelengths 313 ± 10 nm, which is known to include one of the strongest OH* radiation emission peaks. The OH* radical is an important intermediate for many chain branching reactions. Therefore, the ignition timing is defined as the first appearance of the OH* radical in the context of this publication.
Both cameras are angled by 45°, since the investigated spray cone propagates through the measurement volume diagonally. Furthermore, both cameras are synchronized and operated with a recording frequency of 10 kHz. The optical settings are kept constant for all conditions and fuels to achieve a direct comparability between different experiments. Each operation point has been operated for at least 25 consecutive cycles, whereas only the last 20 are stored and post-processed to eliminate effects of heated fuel in the nozzle while adjusting the operation parameters [31][41].

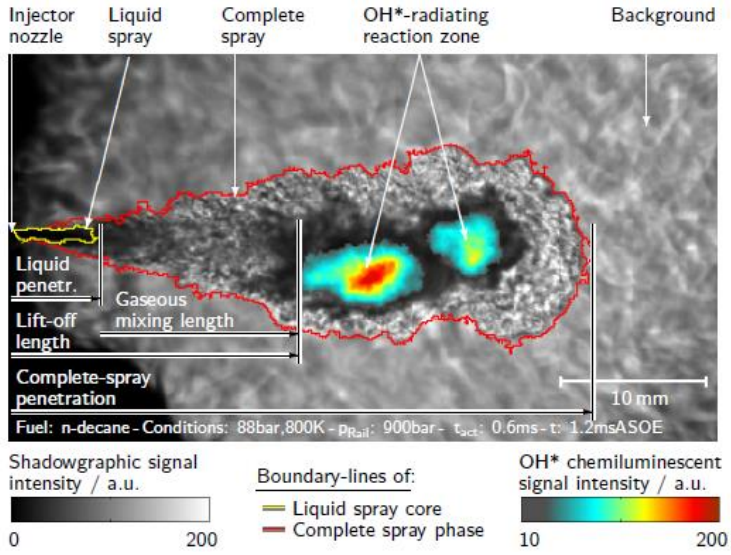

Figure 3. Representative single-shot superposition of the shadowgraphic and OH*-chemieluminescence visualization [31].

A representative single shot image with the superposition of both signals is given in figure 3. Here, all parts in gray-scale intensities are derived from the shadowgraphic visualization whereas the yellow and red boundary lines are added to show the automatically detected edges of the liquid spray core and complete spray. These images allow the determination of liquid and complete spray penetration in axial direction for each recorded time step of the measurement.
In addition to this, the simultaneously recorded OH* signals are superimposed to figure 3 in color scale intensities. Here, it can be seen that two individual OH* radiating areas have been recorded in this exemplary single shot. This shows that the mixture can ignite at different positions simultaneously. The minimum axial distance between the nozzle and the first OH* radiating area is defined as the LOL. An increased lift-off length provides more space for the entrainment of ambient air and therefore is a parameter to qualitatively describe the mixture quality [31]. Here, it is important to note that OH* camera was adjusted to detect these early OH* radiating kernels with high sensitivity. This setting, however, can result in the OH* signal completely saturating during the later stages of flame development as soot radiation appears.

Due to the sensitive OH* camera settings and corresponding soot-OH* cross-talk, the lift-off length are only given for the time of ignition at which soot particles and radiation are not yet formed.

The superposition of the simultaneously recorded shadowgraphic and chemilumiscent images allow the determination of another characteristic length, which is called gaseous mixing length (GML). The GML is the difference between the lift-off length and liquid penetration length at the time of ignition. This parameter is informative since two fuels could achieve identical ignition delay and lift-off but could differ with respect to liquid penetration. In this case, the fuel with less liquid penetration provides more axial distance for air entrainment and mixture preparation until the initial reaction zone is reached. Therefore, a longer GML provides an additional parameter to qualitatively describe the mixture composition at ignition timing. Further results and discussion regarding the GML can be found in [31][41].

3. 1D spray model description

In this section, an overview of the model will be given. A detailed description of a previous version of this model can be found in [22][23][42].

The spray is assumed to be injected into a quiescent air volume, which is large enough so that flow evolution does not modify air conditions far away from the nozzle. Figure 4 shows a sketch of the basic configuration of this type of problem. Fuel stream is assumed to have a uniform velocity profile at the nozzle exit. This flow exchanges momentum with the ambient air and sets it in motion, so that it increases in width with the axial distance. The spray cone half-angle (or spreading angle) $\theta/2$ defines this radial growth, and will be an input to the model. Together with the nozzle diameter d_0, the spray angle defines the virtual origin of the spray in terms of $x_0 = d_0/2/\tan(\theta/2)$.

The spray domain is divided axially into a number of cells with a certain thickness Δx spanning the whole spray cross section. Each cell is limited by the inlet and the outlet sections (i and $i+1$, respectively) so that $x_{i+1} = x_i + \Delta x$. At every time instant, the spray size is defined in terms of the tip penetration s, which is the farthest cell from the nozzle where inlet velocity is different from zero and outlet velocity is zero.

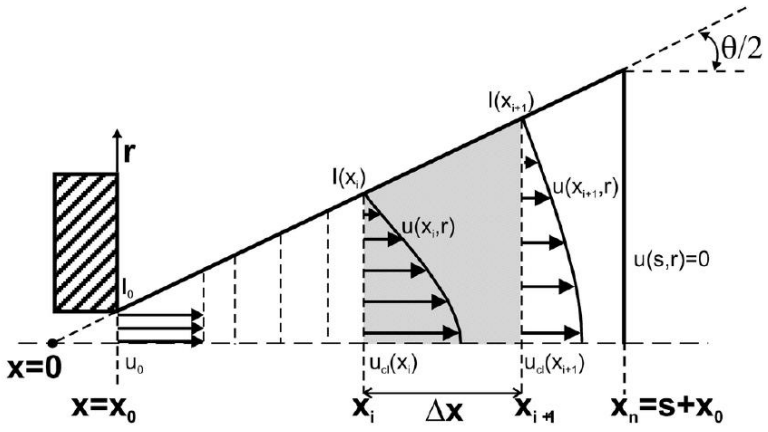

Figure 4. Model description.

The following hypotheses are made:

1. Symmetry on the spray axis, i.e., no air swirl.

2. A fully developed turbulent flow is assumed, which means that self-similar radial profiles can be defined for the conserved variables. In the present approach, a radial Gaussian profile is assumed, so that

$$\frac{u(x,r)}{u_{cl}(x)} = \left[\frac{f(x,r)}{f_{cl}(x)}\right]^{1/Sc} = exp\left[-k\left(\frac{r}{x}\right)^2\right] \quad (1)$$

where $u_{cl}(x)$ and $f_{cl}(x)$ are values on the spray axis of the axial component of the velocity vector and mixture fraction, respectively, k is a constant, and Sc is the turbulent Schmidt number.

3. Linked to the previous assumption, the spray cone angle is defined as the location where the axial velocity is ζ = 1% of the value on the spray axis, so that

$$k = \frac{ln(1/\zeta)}{tan^2(\theta/2)} \quad (2)$$

4.The turbulent Lewis number is assumed to be equal to 1. Consequently, the local enthalpy, for which no conservation equation is solved, can be expressed as

$$h(x,r,t) = h_{a,\infty} + f(x,r,t)\left(h_{f,0} - h_{a,\infty}\right) \quad (3)$$

where $f(x, r, t)$ is the local mixture fraction value and $h_{f,0}$ and $h_{a,\infty}$ are the enthalpy of pure fuel (nozzle outlet conditions) and pure air (far away from the nozzle), respectively. This relationship is independent of the general flow calculations, so that state relationships can be calculated *a priori*, as will be shown below.

5. The pressure is assumed to be constant all over the spray.

6. A locally homogeneous flow is assumed, i.e., local equilibrium exists both in thermal and velocity conditions. This allows for the consideration of the spray as a single-fluid jet.

Conservation equations of axial momentum and fuel mass are formulated for each cell (figure 4), which leads to the following expressions:

$$I(x_i,t) - I(x_{i+1},t) = \frac{d}{dx}\int \rho u dV \quad (4)$$

$$M_f(x_i,t) - M_f(x_{i+1},t) = \frac{d}{dx}\int \rho f dV \quad (5)$$

The terms on the left-hand side of the equations correspond to the conserved property fluxes across the cell inlet and outlet surfaces. Thus, I and M_f stand for the axial momentum (related to local axial velocity, u) and mixture fraction (related to local mixture fraction, f) fluxes,

respectively. The right-hand-side terms represent the temporal variation of the integral over the whole cell, which quantifies the process of accumulation or de-accumulation of momentum and fuel within a cell. By means of corresponding radial integration of self-similar profiles, such equations can be expressed in terms of on-axis unknowns u_{cl} and f_{cl}, which can be solved starting from the nozzle exit, where injection conditions are known. After solving both unknowns, local values of u and f at any radial position can be retrieved from the on-axis properties by means of the corresponding self-similar radial profile.

To solve the previous equations, a definition of local density has to be made. Formally, this is expressed as a function of the type $\rho = f(f)$, which falls into the category of the so-called state relationships. In a more general way, such relationships define the local composition, temperature, and density of the spray in terms of the mixture fraction, by means of ideal adiabatic-mixing processes of pure fuel stream [nozzle conditions, subscripted as $(f, 0)$] and pure air [subscripted as (a, ∞)]. These boundary conditions can be considered either constant or variable with time. Calculation of state relationships is independent of the solution of the flow conservation equation and will be described in the following section.

Figure 5 summarizes the model structure, showing explicitly the link between boundary conditions (inputs for each calculation) and the solution procedure. The conservation equations are solved at each cell, to obtain u_{cl} and f_{cl}, from which u and f can be obtained at any other location. Required information consists of momentum I_0 and mass M_0 fluxes at the nozzle exit, and the radial integration of radial profiles coupled to the local density. To calculate such integrals, the spray cone angle θ is needed (to define the self-similar profile function) as well as the local density ρ, which is obtained from the state relationships module. Eventually, once f is obtained at one location, local temperature, density, and composition can also be calculated from state relationships.

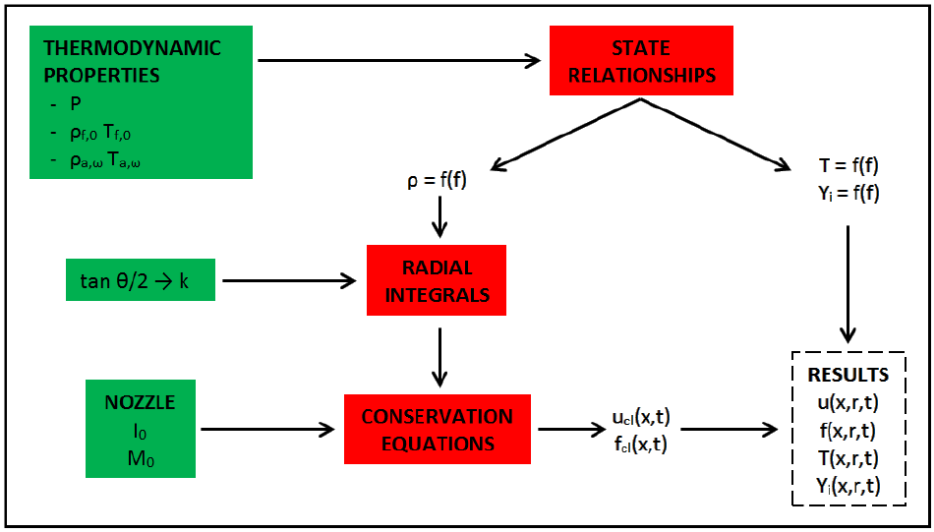

Figure 5. General overview of the model.

4. Results and discussion

4.1. Test conditions

The HPC measurements were performed at the three steady-state operating conditions given in table 3. These conditions were aimed to reproduce the realistic in-cylinder ambient achieved during some of the NEDC tests for an inertia weight class of 1590 kg.

Operating condition	Temperature [K]	Pressure [bar]	Density [kg/m^3]
I	800	50	22
II	800	88	39
III	900	100	39

Table 3. HPC operating conditions.

In particular, the first operating condition is closely comparable to the SCE in part-load operation (n = 1500 rpm, IMEP = 6.8 bar) and the third operation point represents the in-cylinder conditions in higher part-load operation (n = 2280 rpm, IMEP = 9.4 bar). Therefore, the findings from the HPC can be related to the soot measurements in the single-cylinder engine (SCE) at similar conditions. As the first and third operating point differ in ambient temperature and density, an intermediate point with the temperature of the first and density of the third operation was introduced. Thus, the effect of increasing ambient temperature and density on ignition stability and mixture formation quality can be investigated independently. It is interesting to remark that the injection pressure and the energizing time were held constant for all tests at P_{rail} = 900 bar and t_{act} = 0.4 ms, respectively. Finally, each condition was recorded for 20 consecutive cycles, which allowed the determination of the corresponding average and standard-deviation values.

4.2. 1D model validation: Liquid length and vapor penetration

Figure 6 shows the temporal evolution of the liquid length and vapor penetration at operating conditions *I*, *II* and *III*, described in table 3. The results are depicted for both model and experimental measurements. It is interesting to note that the 1D model (DICOM) has been tuned considering the different physical and chemical properties for each fuel shown in table 2. Thus, under these operating conditions, it stated that the 1D model predicts accurately the experimental results independently on fuel type.

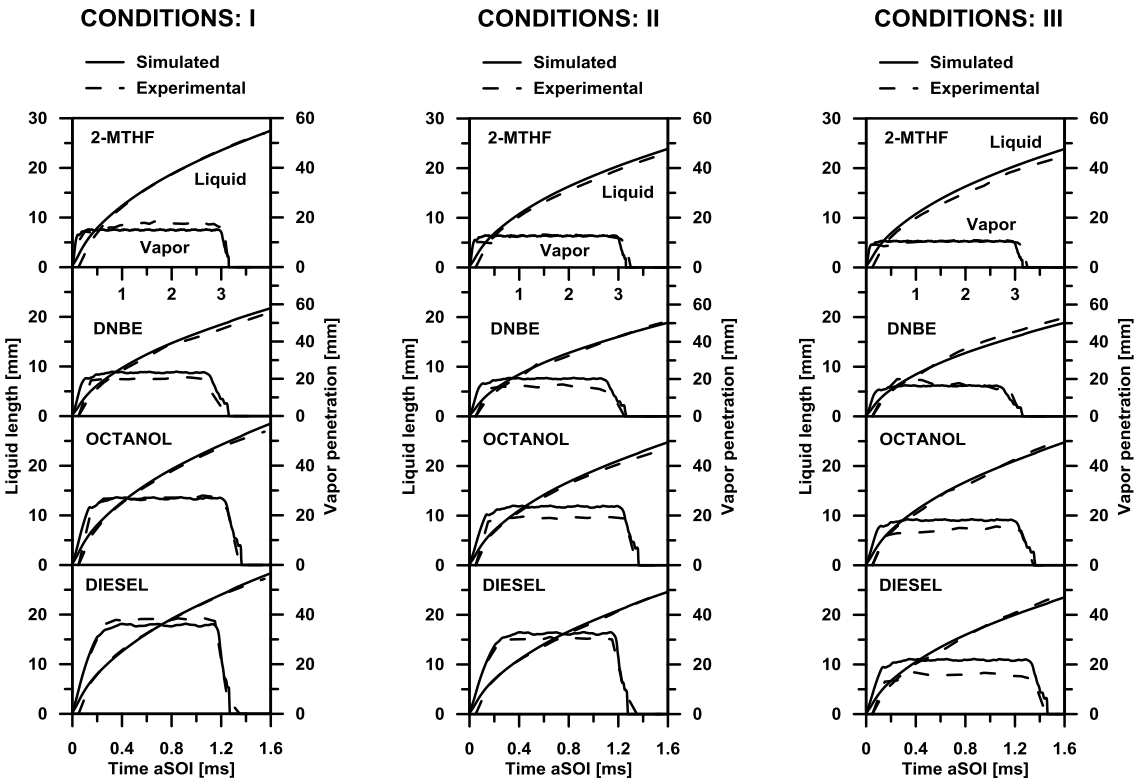

Figure 6. Temporal evolution of the liquid length and vapor penetration for the operating conditions *I*, *II* and *III* depicted in table 3.

Focusing on the experimental results, it is seen the slight influence of fuel type on vapor penetration, leading to very similar values for the same operating conditions. Moreover, it is clear that the largest liquid length is obtained for diesel fuel, followed by 1-octanol and DNBE, being the liquid length of 2-MTHF the shortest one. A detailed explanation of this behavior will be provided in next section. On the other hand, results reveal that the increase in density while keeping constant the temperature (from *I* to *II*), results in shorter vapor penetration independently on fuel type. In this sense, liquid length it is also slightly reduced for all fuels. The increase in temperature (either from *I* to *III*, or from *II* to *III*) causes clear differences in liquid length, becoming shorter as temperature increases. Thus, it is interesting to remark that the hypotheses of the model as well as its tuning for each fuel are valid even modifying strongly the operating conditions.

4.3. Influence of fuel properties on vaporization process: theoretical approach

Considering Desantes et al. [43], it is possible to define the maximum liquid length in steady conditions as:

$$LL = K \cdot \left[d_0 \sqrt{\frac{\rho_f}{\rho_{amb}}} \right] \cdot \frac{1}{Y_{f,evap}} \qquad (6)$$

Where K is the spray constant, d_0 is the nozzle diameter, ρ_f and ρ_{amb} are the fuel and ambient densities respectively, and $Y_{f,evap}$ is evaporated fuel mass fraction.

In equation 6, the term in brackets is widely known in the literature as the “equivalent diameter” and characterizes the spray mixing scales (i.e. momentum). Such “mixing factor” considers both in-cylinder and fuel physics, by including the ratio of fuel and ambient densities. Moreover, the last term of equation 6 is usually referred to as the “energy factor” as it accounts for the spray vaporization processes. It can be rewritten in terms of enthalpies such as in equation 7 and 8.

$$\Delta h_{amb}\left(T_{amb}, T_{evap}\right) \cdot \left(1 - Y_{f,evap}\right) = Y_{f,evap} \cdot \Delta h_f\left(T_{f,0}, T_{evap}\right) \tag{7}$$

$$\frac{1}{Y_{f,evap}} = 1 + \frac{\int_{Tf,0}^{Tevap} C_{pl,f} \cdot dT + L_{v,f}\left(T_{evap}\right)}{\int_{Tevap}^{Tamb,\infty} C_{p,amb} \cdot dT} \tag{8}$$

Where T_{amb} is the ambient gas temperature, $T_{f,0}$ is the initial fuel temperature and T_{evap} is the temperature of saturation when the fuel is entirely vaporized. Additionally, this parameter depends on both fuel properties and ambient thermodynamic conditions [43][44], by involving the specific heat capacity of the liquid fuel ($C_{pl,f}$) and its latent heat of vaporization ($L_{v,f}$) on one hand, and the ambient temperature (T_{amb}) on the other hand. Finally, $C_{p,amb}$ is referred to the specific heat capacity of the ambient and T_0 to initial temperature.

Taking into account these relationships as well as fuel characteristics, the evaporated fuel mass fraction ($Y_{f,evap}$) was calculated for different operating conditions. In particular, the calculations were performed in a density range of 10-60 kg/m^3 and temperature interval of 700-1300 K. The density and temperature ranges were selected as representative of engine conditions. Figure 7 shows the calculated $Y_{f,evap}$ for an ambient temperature sweep maintaining constant density at 10 kg/m^3 (left) and 60 kg/m^3 (right). From the figure it is seen that ambient temperature has a direct impact on $Y_{f,evap,}$ while an inverse relationship is found with density. In addition, 2-MTHF presents the highest $Y_{f,evap}$ for the same conditions, followed by DNBE, 1-octanol and diesel.

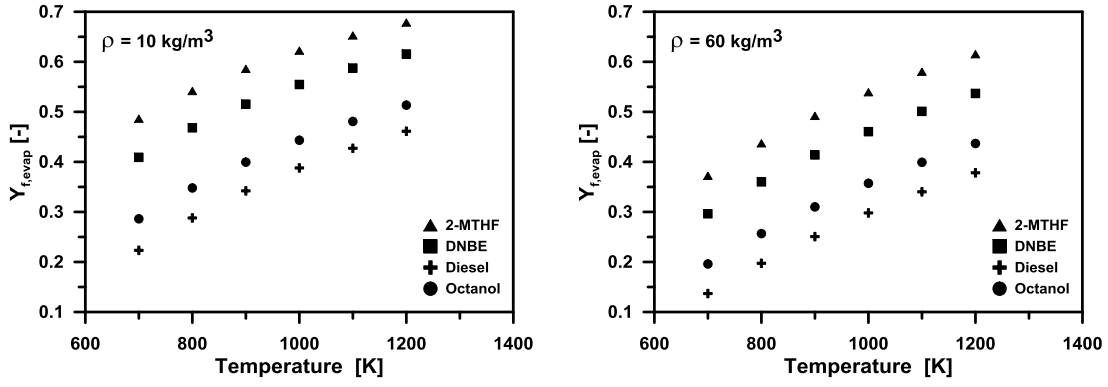

Figure 7. Calculated $Y_{f,evap}$ for an ambient temperature sweep maintaining constant density at 10 kg/m^3 (left) and 60 kg/m^3 (right).

Once determined the $Y_{f,evap}$ for each fuel at desired conditions, considering equation 6 it is possible to define scaling laws for their LL based on diesel LL. For that purpose it is also necessary to know diesel and fuels densities as well as diesel $Y_{f,evap}$ at the same conditions, as shown in equation 9:

$$\frac{LL_{diesel}}{LL_{fuel_i}} = \sqrt{\frac{\rho_{diesel}}{\rho_{fuel_i}}} \cdot \frac{Y_{f,evap_{fuel_i}}}{Y_{f,evap_{diesel}}} \quad (9)$$

In order to validate the analytical expression for the liquid length scaling laws shown in equation 9, figure 8 shows the theoretical LL_{diesel}/LL_{fuel_i} ratio calculated for a temperature sweep at fixed densities as well as the experimental values at the three conditions defined in table 3 (*I*, *II* and *III*).

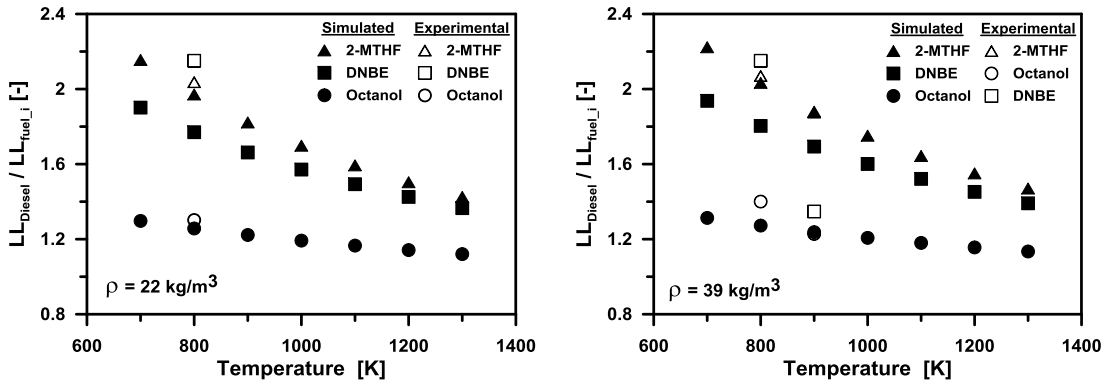

Figure 8. Theoretical versus experimental results of the LL scaling laws. Temperature sweep at constant density of 22 kg/m^3 (left) and 39 kg/m^3 (right).

In the right of the results, it is concluded that the scaling laws predict with enough accuracy the experimental results with respect to 1-octanol and 2-MTHF (note that at 900 K and 39 kg/m^3, experimental and simulated results are colliding). By contrast, some discrepancies are found between experimental measurements and theoretical calculations in the case of DNBE. In this case, the low viscosity of DNBE fuel makes more difficult to distinguish between the gas phase and liquid phase by means of shadowgraphy technique. Hence the error in the determination of the liquid penetration length of DNBE is rather large and is more dependent on the limits set in the image post-processing. As a general conclusion, the maximum LL for each TMFB is shorter than for diesel. Moreover, the differences in LL_{max} are reduced as temperature increases. In this case, the minimum LL_{max} is found with 2-MTHF, followed by DNBE, 1-octanol and diesel.

4.4. Influence of fuel properties on spray mixing

To better understand the effects of fuel type on mixing process, the vapor penetration is studied here. Figure 9a shows the temporal evolution of the experimental vapor penetration as well as its standard deviation for all four fuels. From the analysis of the figure, it is clear that vapor penetration is independent of fuel type. In order to show this behavior, figure 9b depicts the temporal evolution of the difference in vapor penetration for all fuels with respect to the diesel vapor penetration. Thus, it is possible to see how this parameter is in the same order of magnitude than the standard deviation of the experimental measurements.

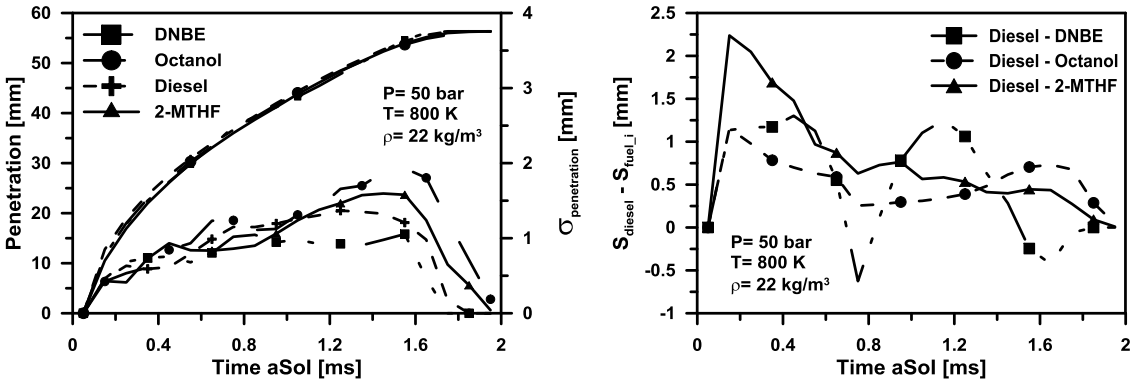

Figure 9. a) Temporal evolution of the vapor penetration and its standard deviation for all the fuels tested (left). b) Temporal evolution of the difference in vapor penetration for all fuels with respect to the diesel vapor penetration (right).

Taking into account theoretical considerations described in [43], it is possible to formulate the vapor penetration as:

$$S = k \cdot M_o^{\frac{1}{4}} \cdot \rho_{amb}^{-\frac{1}{4}} \cdot t^{\frac{1}{2}} \cdot tan^{-\frac{1}{2}}\left(\frac{\theta}{2}\right) \quad (10)$$

Where k is a constant of adjustment, M_o is the spray momentum flux, ρ_{amb} is the ambient density, t is the time and θ the spray cone angle.

Since vapor penetration is almost constant for all the fuels tested in the HPC, it is possible to conclude that the momentum flux and the spray angle are almost constant independently on the fuel used. Thus, the total air entrainment is very similar for all fuels. However, it is interesting to note that the mixture field is defined by fuel properties. In order to evaluate these differences, figure 10 shows the spatial position of different iso-ϕ lines for the different fuels 1 ms after the start of injection for the operating conditions *I*, defined in table 3. From Figure 10 it can be stated that no variation in the mixture field is expected for fuels with the same stoichiometric equivalence ratios (1-octanol and DNBE). In addition, as stoichiometric air-fuel ratio decreases, i.e. as fuel oxygen content increases, the mixture field is located nearer the injector nozzle.

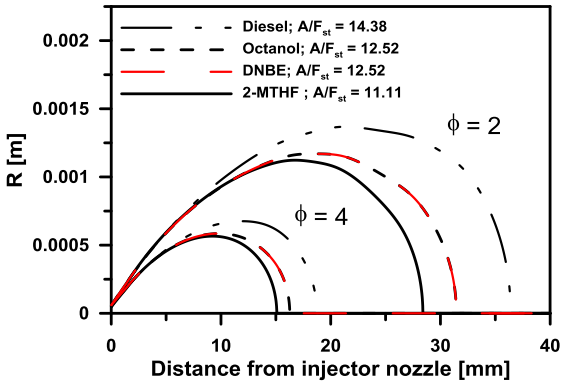

Figure 10. Spatial distribution of the equivalences ratios for the different fuels.

The mixture rate, which is defined as the fuel mass amount mixed to stoichiometric equivalence ratio normalized by the total fuel mass amount, $m_{\phi=1}/m_{inj}$,, has been compared

between fuels with equal stoichiometric equivalence ratio (DNBE and 1-octanol) without considering chemical kinetics effects (under non reacting conditions). For this purpose, 4 ms injection rates were simulated to ensure steady-state conditions. Thus, figure 11a shows the temporal evolution of the mixture rate for DNBE and 1-octanol. In addition, the colliding profiles represented in figure 11b confirmed that mixture rate only depends on the square root of the fuels densities ratio.

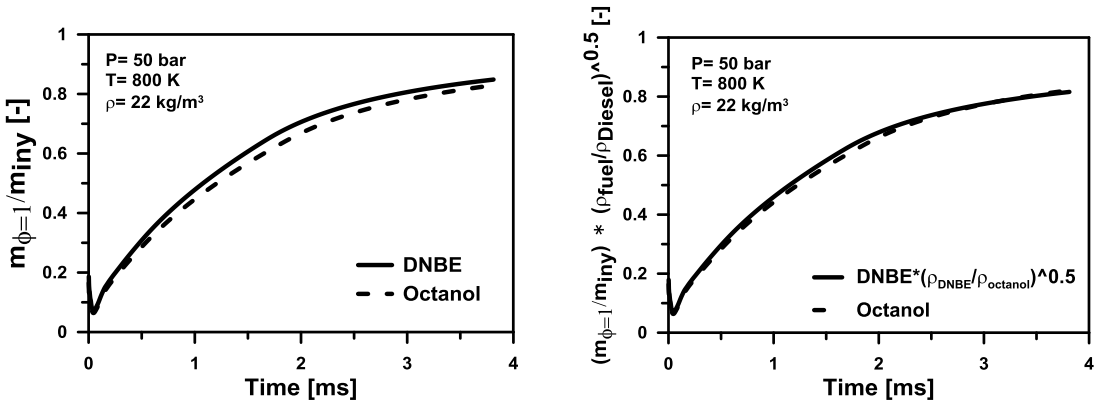

Figure 11. Temporal evolution of the mixture rate for DNBE and 1-octanol (left). Temporal evolution of the mixture rate for DNBE and 1-octanol scaled with the square root of the density ratios of the fuels (right).

In order to add the effect of chemical kinetics to the evaluation of the mixture formation and combustion with the different fuels, the mixture conditions were modelled at the time of the experimental ignition delay, obtained from the tests in the high pressure chamber. Figure 12 presents several pie charts accounting the fuel mass percentage mixed to different equivalence ratios for the three operating conditions evaluated in this research (table 3). Each row of figures correspond to the same operating conditions and present the equivalence ratio distributions for the four fuels investigated. The experimental ignition delay for each fuel is depicted under its corresponding chart. In order to build the different pie charts, five different scenarios have been considered. The first one includes very lean equivalences ratios, $0.1<\phi<0.5$, which cause the main amount of unburned HC and CO emissions. The second, $0.5<\phi<0.9$, accounts the fuel mass mixed to lean equivalences ratios. The third, includes the mass percentage mixed to stoichiometric conditions, $0.9<\phi<1.3$, which governs the autoignition. The next scenario, $1.3<\phi<2.3$, covers the mass mixed to rich equivalences ratios and finally, $\phi>2.3$, which has a strong effect on soot generation. From figure 12, it is noted that an increase in density and temperature promotes shorter ignition delays (ID) whatever the fuel. Thus, the mixture field shows high fuel mass amount mixed to rich equivalence ratios. Focusing on the different fuels at the same thermodynamic conditions, it is clear that as cetane number is increased, shorter ignition delay is obtained. It results in a high fuel mass percentage mixed to rich equivalence ratios.

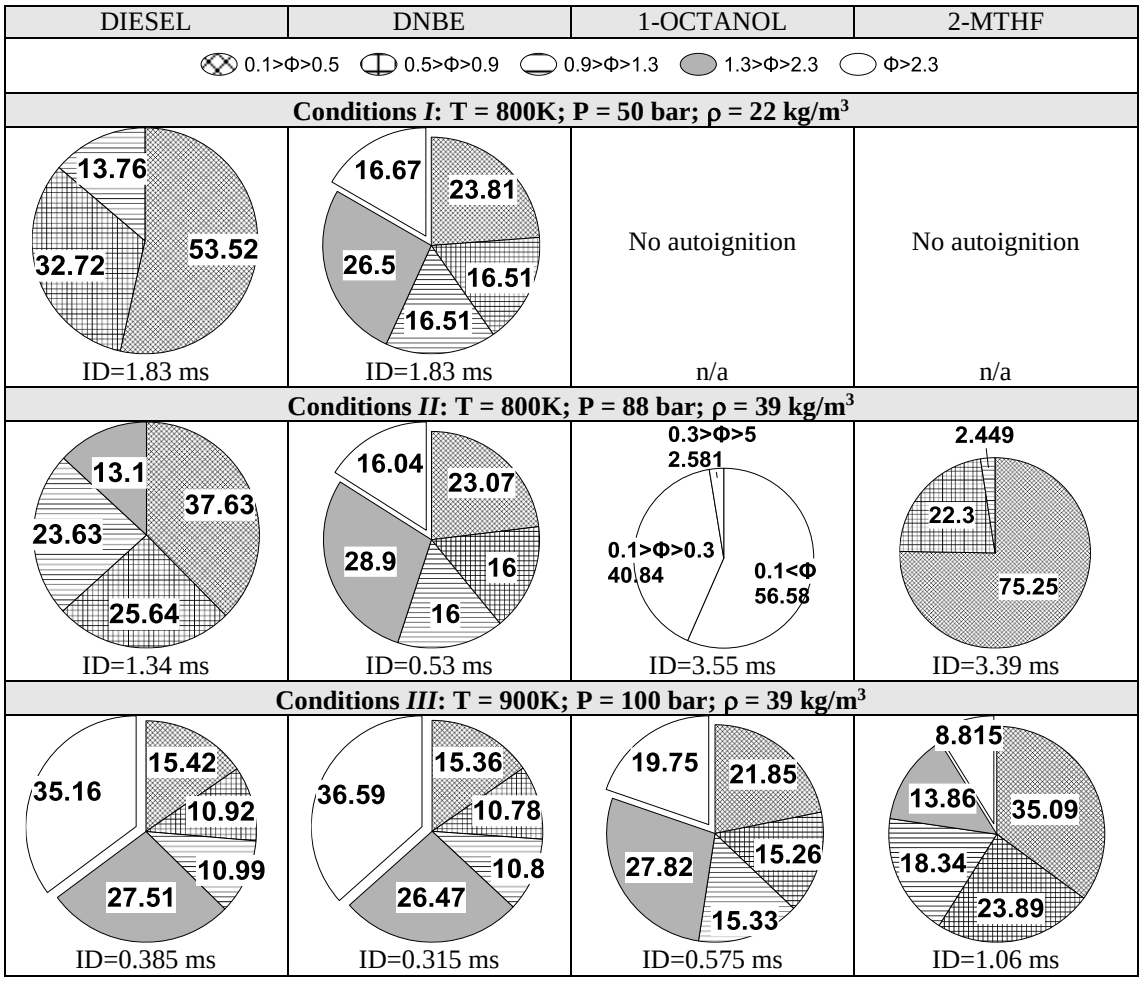

Figure 12. Fuel mass percentage mixed to different equivalence ratios for each fuel in operating conditions *I*, *II* and *III*. Note that 1-octanol does not follow the legend at conditions *II* due to the excessive lean conditions achieved.

Figure 12 focused on the mixing process just at start of combustion timing. However, in order to determine the pollutant emissions, mainly soot emissions, it is necessary to evaluate the mixing process just in a particular position. Thus, figure 13 shows the lift-off length as well as the local equivalence ratio at the lift-off length (ϕ_{LOL}) for the different experimental ignition delays in conditions *II* and *III*.

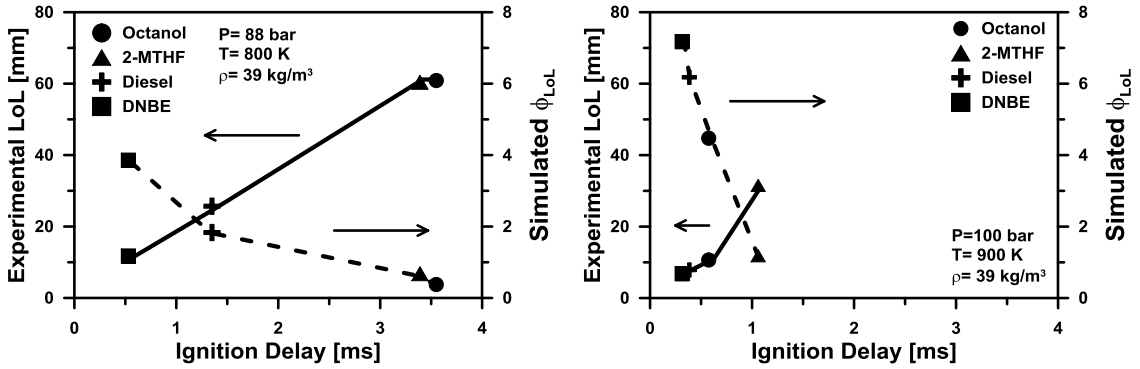

Figure 13. Lift-off length and local equivalence ratio at the lift-off length ϕ_{LOL} for the different experimental ignition delays in conditions *II* and *III*.

Considering both operating conditions presented in the figure, it can be stated that the lift-off length increases as the ignition delay increases resulting in a lower equivalence ratios at the lift-off length (ϕ_{LOL}). On the other hand, as the temperature increases, ignition delay decreases and ϕ_{LOL} increases, which is expected to promote higher soot formation [45].

5. Discussion

In order to validate under realistic conditions the findings extracted from the fundamental study presented above, several soot measurements have been carried out in a single-cylinder engine (SCE). The SCE used for the tests has a compression ratio of 15:1 and has a state-of-the-art series production fuel injection system. In addition, the engine conditions selected for the tests were based on realistic operating conditions, with three of the four tests within the NEDC range for an inertia weight class of 1590 kg [46]. The SCE specifications, engine operating conditions and injection details are summarized in table 5, table 6 and table 7 respectively.

Displacement [cm³]	390
Stroke [mm]	88.3
Bore [mm]	75
Compression ratio [-]	15:1
Valves/cylinders number [-]	4
Max. cylinder pressure [bar]	220
Fuel injection [-]	Piezo Common rail
Max. injection pressure [bar]	2000
Max. boost pressure [bar abs.]	3.8

Table 5. Single-cylinder engine specifications.

Test [-]	Engine speed [rev/min]	IMEP [bar]	CA50 [CAD bTDC]	P_{rail} [bar]	P_{boost} [bar]	$T_{intake\ air}$ [°C]	$P_{exhaust}$ [bar]
1	1500	4.3	-6.6	720	1.07	25	1.13
2	1500	6.8	-5.8	900	1.5	30	1.6
3	2280	9.4	-9.2	1400	2.29	35	2.39
4	2400	14.8	-10.8	1800	2.6	45	2.8

Table 6. Engine operating conditions detail.

Test [-]	SOE [CAD bTDC]				DOI [us]				Fuel injected [mg]			
	Die.	OCT	2-MTHF	DNBE	Die.	OCT	2-MTHF	DNBE	Die.	OCT	2-MTHF	DNBE
1	14.6	19.9	-	7.1	368	391	-	400	9.3	11.1	-	11.3
2	9.3	13	19	6.8	397	444	477	436	15.4	17.6	19.2	17.1
3	7.5	7.7	14.2	7.8	363	406	378	392	19.9	23.3	24.6	21.9
4	9.2	9.2	8.9	9.5	447	506	509	500	30.7	36.5	38.4	35.0

Table 7. Detail of injection settings for the different fuels and test conditions.

Figure 14 (left) presents soot emissions measurements at the four engine operating conditions for all fuels. In this study, an AVL SmokeMeter 415S was used to determine the smoke emissions. To report the FSN into indicated specific particulate matter, a correlation provided by AVL was applied [47]. Note that no ignition is attained for 2-MTHF at 4.3 bar IMEP. In addition, to assess the influence of formation and oxidation processes on final soot emissions, the ratio between ignition delay (ID) and injection duration (DoI) is presented in figure 14 (right). In this sense, the ID/DoI ratio represents the degree of air and fuel mixing. As ID/DoI becomes lower, higher amount of the injection rate is burned under mixing-controlled

conditions. Moreover, ID/DoI values greater than one denote injection and combustion processes decoupled in time, leading to premixed combustion.

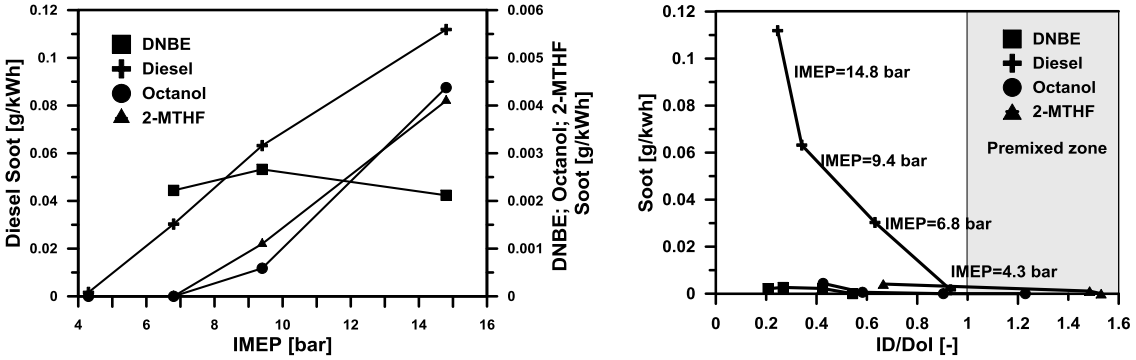

Figure 14. Soot emissions for diesel, 2-MTHF, DNBE and 1-octanol measured at four engine operating conditions (left). Soot emissions for the different fuels versus the ID/DoI ratio (right).

Looking at figure 14 (left), the great reduction in soot levels achieved with the TMFB candidates compared to diesel fuel is clearly confirmed. In the case of 1-octanol and 2-MTHF, the findings from the HPC about the role of soot formation on final emission levels agree with the behavior found in the SCE. Thus, the lower cetane number than diesel fuel resulted in increased ignition delay in the SCE tests, leading to lower soot formation. It is worth noting that no ignition was obtained with 2-MTHF at 4.3 bar IMEP due to the very low cetane number of this fuel. However, the longer ignition delay also causes higher emissions of unburned hydrocarbons and carbon monoxide, as presented in [48][49]. By contrast, the comparison of DNBE/diesel in figure 14 (left) suggests that, in this case, results are not only related to soot formation process. In particular, DNBE allows lower soot emissions than diesel fuel even showing shorter ignition delay. Considering the oxygenated nature of this fuel, not only mixing conditions at lift-off length determine if soot formation is increased or decreased. In any case, the three TMFB candidates are very suitable for mixing-controlled combustion at least from the soot point of view. It is also worthy to note that, at these operating conditions, ID/DoI values greater than one results in almost zero soot emissions whatever the fuel used. The extremely low emissions of PM for the TMFB fuels have also been measure using an Engine Exhaust Particulate Sizer Spectrometer (EEPS) at higher engine loads [50].

6. Conclusions

In the present study, the influence of fuel properties on fundamental spray characteristics has been studied in a high pressure chamber using different tailor-made fuels from biomass. The investigations in the high pressure chamber have revealed that both ambient density and temperature have an impact on fuel vaporization. Moreover, the comparison suggested that temperature is the governing factor. In addition, due to the very high volatility and low density of TMFB, the liquid penetration length of these oxygenated compounds is reduced up to 60% (2-MTHF) compared to Diesel fuel. However, the impact of increasing temperatures is higher at low temperature levels.

Moreover, 1D computational modeling tools have been used to gain a deeper understanding of the fuel/air mixing process with these new fuels. Simulations have proven that under non-reactive conditions, the vapor penetration is similar for all fuels. Therefore, the air entrainment is alike too. Moreover it has been demonstrated that differences in local equivalence ratios mainly originated from stoichiometric air demand variations. Thus, it has been proven that the mixture fraction field for fuels with equal stoichiometric equivalence ratio only depends on the square root of the fuel densities. Under reactive conditions, chemical kinetics dominate the ignition delay, and therefore, the mixing process. Longer ignition delay resulted in increased

lift-off length, thus the mixture has lower equivalence ratio at point of ignition. Thus, the main reasons for the low sooting tendency with TMFB are in the reduced reactivity and in the high oxygen content, both resulting in an almost lean mixture at SOC.

Finally, the potential of the TMFB candidates to reduce soot emissions in realistic SCE conditions has been proven. In this sense, the findings from the HPC about the important role of soot formation on final emission levels agree of 1-octanol and 2-MTHF were validated. Moreover, the mechanisms by which DNBE fuel allows to improve engine-out soot emissions versus diesel fuel should be further studied. Additionally, it was found that even with less degree of air and fuel mixing (ID/DoI lower than diesel fuel), extremely low soot emissions can be reached with any TMFB proposed.

Acknowledgements

This work was performed as part of the Cluster of Excellence “Tailor-Made Fuels from Biomass”, which is funded by the Excellence Initiative by the German federal and state governments. Simulation works have been partially funded by Spanish government under the grant “José Castillejo” (CAS12/000097).

References

[1] Stone R. Introduction to Internal Combustion Engines. Society of Automotive Engineers, Inc., Warrendale, PA, ISBN 978-0-7680-2084-7, 1999.

[2] Johnson, T. Diesel Emissions in Review. SAE Int. J. Engines 4(1):143-157, 2011, doi:10.4271/2011-01-0304.

[3] Palash SM, Masjuki HH, Kalam MA, Masum BM, Sanjid A, Abedin MJ. State of the art of NOx mitigation technologies and their effect on the performance and emission characteristics of biodiesel-fueled Compression Ignition engines. Energy Conversion and Management, Volume 76, December 2013, Pages 400-420.

[4] Liu H, Ma S, Zhang Z, Zheng Z, Yao M. Study of the control strategies on soot reduction under early-injection conditions on a diesel engine. Fuel, Volume 139, 1 January 2015, Pages 472-481.

[5] Hoeven MV. CO2 emissions from fuel combustion highlights. International Energy Agency; 2012.

[6] Thiel C, Schmidt J, Van Zyl A, Schmid E. Cost and well-to-wheel implications of the vehicle fleet CO2 emission regulation in the European Union Transportation Research Part A: Policy and Practice, Volume 63, May 2014, Pages 25-42.

[7] International Energy Agency. World energy outlook 2010. Paris: OECD/IEA; 2010.

[8] U.S. Energy Information Administration. International energy outlook 2010, DOE/EIA-0484(2010), Washington; 2010.

[9] International Energy Agency. Technology roadmap biofuels for transport. Paris: ECD/IEA; 2011.

[10] European Union. DIRECTIVE 2009/28/EC, EU, 23.4.2009; 2009.

[11] Imran A, Varman M, Masjuki HH, Kalam MA. Review on alcohol fumigation on diesel engine: A viable alternative dual fuel technology for satisfactory engine performance and reduction of environment concerning emission. Renewable and Sustainable Energy Reviews, Volume 26, October 2013, Pages 739-751.

[12]Labeckas G, Slavinskas S, Mažeika M. The effect of ethanol–diesel–biodiesel blends on combustion, performance and emissions of a direct injection diesel engine. Energy Conversion and Management, Volume 79, March 2014, Pages 698-720.

[13]Beatrice C, Bertoli C, Del Giacomo N, et al. In-cylinder soot evolution analysis in a transparent research DI diesel engine fed by oxygenated fuels. SAE paper 2002-01-2851, 2002.

[14]Nerva J-G, Genzale C, Kook S, García JM, Pickett L. Fundamental spray and combustion measurements of soy methyl-ester biodiesel. International J of Engine Research 14(4) 373-390.

[15]Janssen A, Müther M, Pischinger S, Kolbeck A, Lamping M. Tailor-Made Fuels: The Potential of Oxygen Content in Fuels for Advanced Diesel Combustion Systems, SAE Technical Paper 2009-01-2765 (2009).

[16]Thewes M, Müther M, Brassat A, Pischinger S, et al. Analysis of the Effect of Bio-Fuels on the Combustion in a Downsized DI SI Engine. SAE Int. J. Fuels Lubr. 5(1):274-288, 2012, doi:10.4271/2011-01-1991.

[17]Janssen A, Müther M, Pischinger S, Kolbeck A, Lamping M, Körfer T. Tailor-Made Fuels for Future Ad-vanced Diesel Combustion Engines, SAE Technical Paper 2009-01-1811 (2009).

[18]Pischinger S, Müther M, Janssen A. Tailor-made Biofuels – Results from the Cluster of Excellence at RWTH, 31. Vienna Motor Symposium (2010).

[19]Janssen A, Kremer F, Baron M, Müther M, Pischinger S, Klankermayer J. Tailor-Made Fuels from Biomass for Homogeneous Low-Temperature Diesel Combustion, Energy Fuels, 25 (10), pp 4734–4744 (2011).

[20]Janssen A, Jakob M, Müther M, Pischinger S. Tailor-Made Fuels Made from Biomass – Potential of Biogenic Fuels for Reducing Emissions, Motortechnische Zeitschrift (MTZ), 12|2010, 71. Jahrgang (2010).

[21]Pepiot-Desjardins P, Pitsch H, Malhotra R, Kirby SR, Boehman AL. Structural group analysis for soot re-duction tendency of oxygenated fuels. Combustion and Flame 154, 191–205(2008).

[22]Pastor JV, López JJ, García JM, Pastor JM. A 1D model for the description of mixing-controlled inert diesel sprays. Fuel, Volume 87, Issues 13–14, October 2008, Pages 2871–2885.

[23]Desantes JM, Pastor JV, García-Oliver JM, Pastor JM. A 1D model for the description of mixing-controlled reacting diesel sprays. Combustion and Flame 2009; 156:234–49.

[24]Pastor JV, García-Oliver JM, Pastor JM, Vera-Tudela W. One-dimensional diesel spray modeling of multicomponent fuels.

[25]Benajes J, Molina S, García A, Monsalve-Serrano J, Durrett R. Conceptual model description of the double injection strategy applied to the gasoline partially premixed compression ignition combustion concept with spark assistance. Applied Energy 2014; 129(15):1–9.

[26]Benajes J, Molina S, García A, Monsalve-Serrano J, Durrett R. Performance and engine-out emissions evaluation of the double injection strategy applied to the gasoline partially premixed compression ignition spark assisted combustion concept. Applied Energy 2014; 134(1):90–101.

[27]Musculus, M. and Kattke, K., "Entrainment Waves in Diesel Jets," SAE Int. J. Engines 2(1):1170-1193, 2009, doi:10.4271/2009-01-1355.

[28]Naber J, Siebers D. Effects of gas density and vaporization on penetration and dispersion of diesel sprays. SAE transactions, vol. 105, pp. 82-111, 1996.

[29]Mancaruso E, Marialto R, Sequino L, Vaglieco B. Comparison of Spray Characteristics Measured in an Optical Single Cylinder Diesel Engine with 1D Model. SAE Technical Paper 2014-01-1424, 2014, doi:10.4271/2014-01-1424.

[30]Finesso R., Spessa E., Mancaruso E., Sequino L., and Vaglieco B. M., "Assessment of a new quasi-dimensional multizone combustion model for the spray and soot formation analysis in an optical single cylinder diesel engine," in ICE2013, Capri, Italy, 2013.

[31]Jakob M. Optical investigations of diesel engine related combustion processes. Doctoral Theses, RWTH, 2014, urn:nbn:de:hbz:82-opus-52561.

[32]Julis J, Leitner W. Selective conversion of biomass-derived platform chemicals to 1-octanol and 1,1-dioctylether. Angew. Chem. Int. Ed. 51, pp. 8615-8619, 2012.

[33]Phanopoulos A, White A, Long NJ, Miller PW. Catalytic Transformation of Levulinic Acid to 2-Methyltetrahydrofuran Using Ruthenium-N-Triphos Complexes. ACS Catalysis, 2015, 5 (4), pp 2500–2512.

[34]Park DS, Yun D, Choi Y, Kim TY, Oh S, Cho J-H, Yi J. Effect of 3D open-pores on the dehydration of n-butanol to di-n-butyl ether (DNBE) over a supported heteropolyacid catalyst. Chemical Engineering Journal, Volume 228, 15 July 2013, Pages 889-895.

[35]Gestis Stoffdatenbank. http://gestis.itrust.de.

[36]NIST Webbook. http://webbook.nist.gov/chemistry.

[37]Carl L. Yaws, Thermophysical Properties of Chemicals and Hydrocarbons, William Andrew 2008

[38]Murphy M, Taylor J, McCormick R. Compendium of Experimental Cetane Number Data, 2004.

[39]Yaws C. Transport Properties of Chemicals and Hydrocarbons, William Andrew 2009.

[40]Pauls Ch, Gruenefeld G, Vogel S, Peters N. Combined simulations and OH chemiluminescence meas-urements of the combustion process using different fuels under diesel-engine like conditions. SAE technical paper 2007-01-0020 (2007).

[41]Jakob M, Klein D, Graziano B, Kremer F, Pischinger S. Simultaneous Shadowgraphic and Chemiluminescent Visualization to Determine the Mixture Formation Quality and ignition Stability of Diesel Engine Related Surrogate Fuels, 14. Tagung "Der Arbeitsprozess des Verbrennungsmotors" (2013).

[42]Pastor JV, López JJ, García JM, Pastor JM. A 1D model for the description of mixing-controlled inert diesel sprays. SAE paper 2005-01-1126; 2005.

[43]Desantes JM, Pastor JV, Payri R, Pastor JM. Experimental characterization of internal nozzle flow and diesel spray behavior. Part II: Evaporative conditions. Atomization Sprays, Vol. 15, pp. 517-43, 2005.

[44]Higgins BS, Mueller CJ, Siebers D. Measurements of fuel effects on liquid-phase penetration in DI sprays. SAE Paper 1999-01-0519, 1999.

[45]Pickett LM, Siebers DL. Soot in diesel fuel jets: effects of ambient temperature, ambient density, and injection pressure. Combustion and Flame 138 (2004) 114–135.

[46]Heuser B, Jakob M, Kremer F, Pischinger S, Kerschgens B, Pitschet H. Tailor-Made Fuels from Biomass: Influence of Molecular Structures on the Exhaust Gas Emissions of Compression Ignition Engines. SAE Technical Paper 2013-36-0571, 2013, doi:10.4271/2013-36-0571.

[47]AVL, Smoke Value Measurements with the Filter Paper Method, Application Notes, June 2005, AT1007E, Rev. 02.

[48]Heuser B, Kremer F, Pischinger S, Klankermayer J. Optimization of Diesel Combustion and Emissions with Tailor-Made Fuels from Biomass. *SAE Int. J. Fuels Lubr.* 6(3):922-934, 2013, doi:10.4271/2013-24-0059

[49]Heuser B, Mauermann P, Wankhade R, Kremer F, Pischinger S. Combustion and emission behavior of linear C8-oxygenates. International Journal of Engine Research, August 2015; vol. 16, 5: pp. 627-638.

[50]Heuser B, Laible T, Jakob M, Kremer F, Pischinger S. C8-Oxygenates for Clean Diesel Combustion. SAE Technical Paper 2014-01-1253, 2014, doi:10.4271/2014-01-1253.

Abbreviations

1D: one dimensional

2-MTHF: 2-methyltetrahydrofuran

CO: carbon monoxide

DNBE: Di-n-butyl ether

HC: hydrocarbon

HPC: high pressure chamber

ID: ignition delay

IMEP: indicated mean effective pressure

LL: liquid length

LOL: lift-off length

SCE: single cylinder engine

SOC: start of combustion

TMFB: Tailor-made fuels from biomass